Content Controlled Spectral Indices for Detection of Hydrothermal Alteration Minerals Based on Machine Learning and Lasso-Logistic Regression Analysis

Kyuhun Shim, Jaehyung Yu, Lei Wang, Sangin Lee, Sang-Mo Koh, and Bum Han Lee

***Abstract*—This article introduced the quantity controlled spectral indices working at mineral contents higher than 5 wt.% for detection of sericite, chlorite, and pyrophyllite, which are the representative alteration minerals of phyllic, propylitic, and advanced argillic hydrothermal alterations. The X-ray diffraction analysis revealed that the samples are mostly pure with minor content of quartz. The absorption features of target minerals showed systematic decrease in absorption depth with decrease in the mineral content, and the changes varied by mineral types. A total of 1253 target mineral spectra and 605 nontarget mineral spectra were classified by a random forest model, which achieved an overall accuracy of 97% with mineral content above 5 wt.%. Least absolute shrinkage and selection operator logistic regressions employed spectral variables of 82 bands for sericite, 132 bands for chlorite, and 84 bands for pyrophyllite with minimal spectral overlap. The overall accuracies were higher than 93.6% with R^2 values ranging from 0.57 to 0.71. Because both target minerals and nontarget minerals, these indices can reliably make mineral classification. To be compatible with remote sensing images, the water-absorption bands were excluded from the indices.**

***Index Terms*—Chlorite, hydrothermal alteration minerals, least absolute shrinkage and selection operator (LASSO) logistic regression, pyrophyllite, quantity controlled indices, random forest (RF), sericite, spectroscopy.**

I. Introduction

HYDROTHERMAL alteration zones have been considered as main exploration targets of mineral resources due to their characteristic distribution surrounding the ore bodies especially for hydrothermal ore deposits [1]–[4]. The hydrothermal alteration zone occurs around ore bodies manifested by zoning of alteration minerals as a result of interaction between host rock and hydrothermal fluid originated from magmatic activities [3], [5]. Due to the characteristic interaction, the hydrothermal alteration zones are distributed systematically around ore bodies, and thus, the identification of specific alteration zone provides critical information about the mineralized areas [6]–[9]. In general, there are nine types of hydrothermal alterations used for mineral resources exploration including argillic, advance agillic, phyllic, propylitic, postassic, greisen, chloritization, silicification, and carbonitization [10], [11]. Among hydrothermal alterations types, phyllic, propylitic, and advanced argillic alterations are main exploration targets because they occur for the most of hydrothermal ore deposit and show systematic zoning with ore bodies [12]–[15]. The phyllic alteration can be defined by assemblages of altered minerals, such as sericite and pyrite where sericite is the main indicator of the alteration [16], [17]. The propylitic alteration is defined by chlorite, epidote, albite, calcite, actinolite, and pyrite, and chlorite and epidote are mostly found in the alteration [6], [18]. Advanced argillic alteration is composed of quartz, alunite, pyrophyllite, dickite, kaolinite, diaspore, andalusite, and corrundum where pyrophyllite and kaolinite are the representative minerals [19]. These alterations zones show various spatial distribution up to kilometers around volcanogenic massive sulfide (VMS), for iron-oxide-copper-gold deposit, and porphyry copper deposits and high sulfidation epithermal gold deposit [6], [20]–[26]. On the other hand, the host rock of hydrothermal ore deposit shows large variations because the hydrothermal deposit often occurs along the geological structures, such as faults and folds. However, the mineral composition of granite includes the most commonly found rock forming minerals in continental environment, such as quartz, feldspar, and mica.

Since 1990s, remote sensing and spectroscopic approaches to mapping hydrothermal alteration have been explored from various platforms such as satellites [26]–[30], airplanes [31]–[33], unmanned aerial vehicle (UAV hereafter) [34], [35], and ground based spectroscopy [36]–[40]. Among the works, ASTER and Landsat-8 band ratios have been found useful for the alternation detection. They were used to map argillic, phyllic, propylitic alternations in epithermal deposit, porphyry copper deposit developing alteration mineral indices including OH-bearing

Manuscript received April 29, 2021; revised June 3, 2021; accepted July 1, 2021. Date of publication July 16, 2021; date of current version August 4, 2021. This work was supported in part by the National Research Council of Science and Technology (NST) grant by the Korea Government (MSIT) under Grant CRC-15-06-KIGAM and in part by the National Research Foundation (NRF) of Korea grant by the Korean Government (NRF- 2020R1A2C2005439). (*Corresponding author: Jaehyung Yu.*)

Kyuhun Shim is with the Department of Astronomy, Space-Science and Geology, Chungnam National Universit, Daejeon 34134, South Korea (e-mail: ssimgga@naver.com).

Jaehyung Yu is with the Department of Geological Sciences, Chungnam National Universit, Daejeon 34134, South Korea (e-mail: jaeyu@cnu.ac.kr).

Lei Wang is with the Department of Geography and Anthropology, Louisiana State Universit, Baton Rouge, LA 70803 USA (e-mail: leiwang@lsu.edu).

Sangin Lee is with the Department of Information and Statistics, Chungnam National University, Daejeon 34134, South Korea (e-mail: sanginlee44@gmail.com).

Sang-Mo Koh and Bum Han Lee are with the Convergence Research Center for Development of Mineral Resources, Korea Institute of Geoscience and Mineral Resources, Daejeon 34132, South Korea (e-mail: kohsm@kigam.re.kr; leebh@kigam.re.kr).

Digital Object Identifier 10.1109/JSTARS.2021.3095926

minerals index, pyrophyllite index, kaolinite index, alunite index, and calcite index [26], [29], [30], [41]–[43]. Machine learning approaches using Hyperion imagery and field data on alteration mapping were reported for Darrehzar porphyry copper deposit for detecting propylitic, argillic, phyllic alteration zones, where neural network (NN) and support vector machine (SVM) classified the alteration zone with accuracies ranging from 78% to 90% [27], [28].

Aerial hyperspectral images were also used to detect hydrothermal alteration zones. Molan *et al*. [32] mapped hydrothermal alteration minerals of Cu-Au porphyry system using the matched filtering algorithm on Hymap hyperspectral images with 56% accuracy. Tripathi and Govil [33] employed AVIRIS-NG hyperspectral images to map the distribution of clay and iron oxide minerals based on spectral angle mapper (SAM) and spectral feature fitting algorithms. Jakob *et al*. [34] used VNIR hyperspectral images acquired from UAV to classifying altered shale, gossan, vegetation, concrete, massive sulfide, and river sediment at abandoned mines in Spain and Czech Republic. Kirsch *et al*. [35] used VNIR-SWIR-LIR UAV images and ground truth data and classified host rocks and alteration minerals including white mica, chlorite, kaolinite, and calcite employing SAM classification.

Ground-based spectroscopic analyses for alteration mineral identification were also reported. Taylor [37] detected hydrothermal alteration minerals including chlorite, actinolite, talc, micas, kaolinite, dolomite, siderite, calcite, and goethite from drilling core samples using commercial software with R^2 ranging from 0.01 to 0.45. Calvin and Pace [39] classified aluminum phyllosilicates, Fe-Mg phyllosilicates, epidote, and silicate minerals from drilling core samples using analytical spectral devices (ASD) mineral identification software. Kruse [36] spectroscopically analyzed kaolinite, illite, chlorite, and montmorillonite based on SAM and linear spectral unmixing algorithms. Acosta *et al*. [40] classified gypsum, muscovite, and chlorite in drilling cores for mineralized area based on random forest (RF) and SVM using mineralogical analysis and VNIR-SWIR hyperspectral data.

In a natural condition, the alteration minerals are mixed with rock forming minerals at various quantities, and, thus, detection of specific alteration minerals by spectrometers is dependent on the spectral absorption by specific minerals under various mixture conditions. However, the previous studies did not consider spectral signals associated with mineral combination and quantity of alteration minerals [27], [28], [32], [34], [35], [37], [39], [40]. Moreover, most of the previous studies rely on the spectral libraries regardless of the fact that the natural occurrence of mineral is beyond the scope of library collections [30], [33], [36], [41]–[43]. This study introduces spectral indices for hydrothermal mineral detection with consideration of mineral combination at various amount for sericite, chlorite, pyrophyllite, and granite, which are the representative alteration minerals of phyllic, propylitic, advanced argillic hydrothermal alterations, and rock forming minerals. The definition of sample minerals and granite was analyzed by X-ray diffraction (XRD) analysis of microscopic observation. The spectral variations of target samples at various proportion of mineral mixture with granite was analyzed. The spectral variables were selected by a RF model, and from which the indices were derived by least absolute shrinkage and selection operator (LASSO) logistic regression models. The RF classification and LASSO logistic regression models were validated with both experimental samples and spectral libraries for the assessment of real-world application.

II. Materials and Methods

A. Sample Preparation and Preprocessing

To control the variations in spectral signals manifested by variations in weight percent of alteration minerals including sericite, chlorite, and pyrophyllite mixed with major felsic igneous rock forming minerals, the representative samples of those minerals and granite samples were powdered with Vibrating Cup Mill Pulverisette 9. The powered samples were then sieved with 200 mesh sieve to remove granulated particle effect [44]. The preprocessed samples were mixed at various weight percent with powered granite samples (see Table I). The proportion of an individual mineral and granite sample is controlled at 5% interval from 0 to 100%. For the case of two or more combination of the alteration minerals, the weight percent of granite was set to 60 wt.% where the rest 40 wt.% was shared by alteration minerals. The total number of samples used in this study was 105 including 61 for individual alteration mineral, 21 for two alteration mineral combination, and 21 for the three alteration mineral cases (see Table I).

B. Validation of Alteration Mineral and Granite Samples

The validation of alteration minerals used in this study was conducted by X-ray diffraction analysis. XRD is commonly used for mineral identification in geological applications [45]. The X-ray diffraction pattern of the alteration mineral samples was acquired by Rigaku Ultima IV XRD with measurement condition of Cu-Ka1(1.5406 Å), 30 mA, 40 kV at 0.02 interval. The XRD pattern was analyzed by Match! Software (Crystal Impact). A thin section was made from the granite sample and microscopically observed. The microscopic analysis identified major rock forming minerals and their proportion in the granite sample, and the granite sample was validated based on mineral proportion.

C. Spectroscopic Analysis

The spectral reflectance of samples was acquired by ASD Labspec 5100 spectrometer. The spectrometer acquires reflectance spectra ranging 350–2500 nm at 3–6 nm resolution. The 350–2500 nm spectral bands are commonly used for characterization of mineral properties such as color, chemical bonding, and chemical component based on absorption features and spectral patterns [38], [46]–[48]. The spectroscopic analysis has been widely used for mineral exploration due to its advantages on nondestructive and prompt acquisition of analysis [23], [39], [47], [49].

The reflectance spectra of powered samples were measured at the mug-light mode five times for each data and averaged. Then, the spectra were smoothed by the Savitski–Golay algorithm using Unscrambler X software to remove noise. The reflectance

TABLE I
SAMPLE PROPORTION (WT. %) OF ALTERATION MINERALS AND GRANITE USED IN THIS ARTICLE

Case	*Gra(wt.%)	*Seri(wt.%)	Case	Gra(wt.%)	*Chlo(wt.%)	Case	Gra(wt.%)	*Pyro(wt.%)
1	100	0	22	100	0	43	100	0
2	95	5	23	95	5	44	95	5
3	90	10	24	90	10	45	90	10
4	85	15	25	85	15	46	85	15
5	80	20	26	80	20	47	80	20
6	75	25	27	75	25	48	75	25
7	70	30	28	70	30	49	70	30
8	65	35	29	65	35	50	65	35
9	60	40	30	60	40	51	60	40
10	55	45	31	55	45	52	55	45
11	50	50	32	50	50	53	50	50
12	45	55	33	45	55	54	45	55
13	40	60	34	40	60	55	40	60
14	35	65	35	35	65	56	35	65
15	30	70	36	30	70	57	30	70
16	25	75	37	25	75	58	25	75
17	20	80	38	20	80	59	20	80
18	15	85	39	15	85	60	15	85
19	10	90	40	10	90	61	10	90
20	5	95	41	5	95	62	5	95
21	0	100	42	0	100	63	0	100

Case	Gra(wt.%)	Seri(wt.%)	Chlo(wt.%)	Pyro(wt.%)	Case	Gra(wt.%)	Seri(wt.%)	Chlo(wt.%)	Pyro(wt.%)
64	60	35	5	0	85	60	25	10	5
65	60	35	0	5	86	60	25	5	10
66	60	5	35	0	87	60	10	25	5
67	60	5	0	35	88	60	10	5	25
68	60	0	35	5	89	60	5	25	10
69	60	0	5	35	90	60	5	10	25
70	60	30	10	0	91	60	20	20	0
71	60	30	0	10	92	60	20	0	20
72	60	10	30	0	93	60	0	20	20
73	60	10	0	30	94	60	20	15	5
74	60	0	30	10	95	60	20	5	15
75	60	0	10	30	96	60	15	20	5
76	60	30	5	5	97	60	15	5	20
77	60	5	30	5	98	60	5	20	15
78	60	5	5	30	99	60	5	15	20
79	60	25	15	0	100	60	20	10	10
80	60	25	0	15	101	60	10	20	10
81	60	15	25	0	102	60	10	10	20
82	60	15	0	25	103	60	15	15	10
83	60	0	25	15	104	60	15	10	15
84	60	0	15	25	105	60	10	15	15

*Gra = Granite, Seri = Sericite, Chlo = Chlorite, Pyro = Pyrophyllite

TABLE II
NUMBER OF SAMPLE AND LIBRARY SPECTRA USED FOR MODEL DEVELOPMENT AND VALIDATION

# of Sericite Spectra		# of Chlorite Spectra		# of Pyrophyllite Spectra	
Sericite 5%	44	Chlorite 5%	44	Pyrophyllite 5%	44
Sericite 10%	39	Chlorite 10%	39	Pyrophyllite 10%	39
Sericite 15%	34	Chlorite 15%	34	Pyrophyllite 15%	34
Sericite 20%	29	Chlorite 20%	29	Pyrophyllite 20%	29
Sericite 25%	24	Chlorite 25%	24	Pyrophyllite 25%	24
Sericite 30%	19	Chlorite 30%	19	Pyrophyllite 30%	19
Sericite 35%	20	Chlorite 35%	20	Pyrophyllite 35%	20
Sericite 40%	20	Chlorite 40%	20	Pyrophyllite 40%	20
Sericite 45%	20	Chlorite 45%	20	Pyrophyllite 45%	20
Sericite 50%	20	Chlorite 50%	20	Pyrophyllite 50%	20
Sericite 55%	20	Chlorite 55%	20	Pyrophyllite 55%	20
Sericite 60%	20	Chlorite 60%	20	Pyrophyllite 60%	20
Sericite 65%	20	Chlorite 65%	20	Pyrophyllite 65%	20
Sericite 70%	20	Chlorite 70%	20	Pyrophyllite 70%	20
Sericite 75%	20	Chlorite 75%	20	Pyrophyllite 75%	20
Sericite 80%	20	Chlorite 80%	20	Pyrophyllite 80%	20
Sericite 85%	20	Chlorite 85%	20	Pyrophyllite 85%	20
Sericite 90%	20	Chlorite 90%	20	Pyrophyllite 90%	20
Sericite 95%	20	Chlorite 95%	20	Pyrophyllite 95%	20
Sericite 100%	20	Chlorite 100%	20	Pyrophyllite 100%	20
Sericite Library	63	Chlorite Library	81	Pyrophyllite Library	24
Total	532	Total	550	Total	493

spectra were transformed with Hull-Quotient correction to analyze absorption features of samples [47], [50]. The spectral analysis was performed by ENVI 4.8 and The Spectral Geologist 7.5(TSG 7.5) software with United States Geological Survey (USGS) and Jet Propulsion Laboratory (JPL), NASA ASTER spectral library.

D. Classification Model Development

1) Calibration and Validation Data Selection: A total of 1120 spectra at various proportion of minerals mixture were used for spectral analysis and derivation of mineral index (see Table II). Moreover, 738 mineral spectra from JPL and USGS spectral library were additionally employed for the model assessment to rigorously test the index applicable for real cases (see Table II) [51], [52]. The library mineral spectra include rock forming minerals, hydrothermal alteration minerals, and ore minerals, which are considered as most of possible minerals occur in a natural condition including alunite, bornite, brucite, calcite, dolomite, chalcopyrite, chlorite, dickite, epidote, fluorite, gypsum, illite, jarosite, kaolinite, montmorillonite, muscovite, pyrophyllite, quartz, tourmaline, etc. The calibration models were developed based on the 70% of sample spectra and library spectra of target minerals, and the rest 30% of sample spectra and library spectra of nontarget minerals were used for validation.

2) Training Data Selection for Index Development by RF: To assess detection efficiency of minimum mineral content for hydrothermal alteration minerals including sericite, chlorite, and pyrophyllite, this article classified 1858 mineral spectra based on the RF algorithm with training set including various amount of each mineral. Because the experimental spectra include mineral samples with target mineral content ranging from 5 wt.% to 100 wt.% in addition to library spectra of various mineral, the 1858 spectra were classified into 20 RF models with training data at an interval of 5 wt.% for each target mineral (see Table III). Based on the accuracy assessment of the 20 RF models, the optimal training set for target mineral detection was selected. In the field condition, spectral signatures of minerals are often affected by strong atmospheric absorption in some spectral regions, which result in low signal-to-noise ratio in these regions [53]. Therefore, this study excluded the major atmospheric absorption bands for development of RF and LASSO-logistic regression.

TABLE III
ACCURACY ASSESSMENT OF RF CLASSIFICATION ON VARIOUS PROPORTION OF SERICITE, CHLORITE, AND PYROPHYLLITE

Training Set	Sericite Model Sericite data #: 532 Non-sericite data #: 1326			Chlorite Model Chlorite data #: 547 Non-chlorite data #: 1326			Pyrophyllite Model Pyrophyllite data #: 493 Non-prophyllite data #: 1365		
	Overall Accuracy[%]	Omission Error[%]	Commission Error[%]	Overall Accuracy[%]	Omission Error[%]	Commission Error[%]	Overall Accuracy[%]	Omission Error[%]	Commission Error[%]
5 wt.%	97.5	2.3	2.6	98.5	4.0	0.5	97.0	3.7	2.7
10 wt.%	95.5	9.8	2.3	95.2	10.4	2.5	95.6	11.2	1.9
15 wt.%	94.0	16.5	1.8	93.0	18.8	2.1	93.7	18.3	2.1
20 wt.%	91.6	25.9	1.4	91.7	24.5	1.6	90.7	28.2	2.4
25 wt.%	90.0	31.2	1.4	90.3	29.3	1.6	89.3	34.3	2.1
30 wt.%	88.3	35.3	2.3	88.8	33.6	1.9	88.4	38.3	2.0
35 wt.%	87.5	38.5	2.1	87.9	37.3	1.5	87.5	41.4	2.1
40 wt.%	86.7	41.5	2.0	86.6	40.6	2.1	86.7	45.8	1.6
45 wt.%	86.0	43.4	2.2	85.5	45.0	1.8	85.4	49.9	1.9
50 wt.%	85.3	48.7	1.1	84.2	47.7	2.4	84.6	52.9	1.9
55 wt.%	83.0	52.8	2.6	82.7	53.6	2.2	84.0	55.8	1.7
60 wt.%	82.8	57.0	1.3	82.4	55.8	1.7	83.0	59.0	1.8
65 wt.%	81.3	60.5	1.9	81.6	57.4	2.1	82.0	64.5	1.2
70 wt.%	80.5	63.5	1.9	80.1	62.5	2.1	81.4	68.2	0.7
75 wt.%	79.5	67.9	1.5	79.9	65.8	1.1	80.4	72.2	0.6
80 wt.%	78.5	72.9	0.8	78.4	70.6	1.2	79.3	76.7	0.4
85 wt.%	77.4	74.4	1.8	77.4	74.0	1.1	78.3	81.3	0.1
90 wt.%	76.5	78.6	1.4	75.9	78.4	1.4	77.1	85.4	0.3
95 wt.%	75.5	82.1	1.4	75.6	81.2	0.8	76.1	90.1	0.1
100 wt.%	74.1	87.8	1.1	73.9	86.5	0.9	75.4	92.5	0.1
Library	73.6	85.0	2.9	74.1	85.4	1.1	75.2	93.3	0.0

The RF algorithm is one of the most used machine learning algorithms that are based on ensemble learning for classification and regression analyses [54]–[56]. It provides variable importance assessment by the Gini index and mean decrease accuracy [57]. The Gini index, also called impurity index, is used for testing how important a viable is in a decision tree. The higher the Gini index, the more important the variable will be in constructing decision trees. The mean decrease accuracy evaluates the accuracy reduction by excluding a variable each time, where the more decrease in accuracy indicates a more important variable [58]. Tree ensembles are constructed based on bootstrap, which uses random sampling on both samples and variables [54]. The RF selects 2/3 of samples as training set (known as "in-bag") and the rest samples (known as "out-of-bag") as test set, and evaluates the classification accuracy by cross-validation [54]. The randomly selected subset of variables is constructed by user-defined number of features ("Mtry"), and the model grows as user-defined number of trees ("Ntree"). The final classification concludes based on the majority votes of all trees. This study used 500 for Ntree and square root of the number of input variables for Mtry [59], [60].

3) Logistic Regression With LASSO: Machine learning algorithms often outperform other regression models. However, the classifiers are not shared by different case studies. To develop a more generalizable model, the training data selected by RF model were used to build mineral indices from logistic regression models. The models were then tested by the least absolute shrinkage and selection operator. The most useful mineral indices for target mineral detection were analyzed by LASSO, and the logistic regression models using the selected spectral variables for sericite, chlorite, and pyrophyllite were derived [61]. LASSO is a popular penalized method that can perform parameter estimation and variable selection simultaneously. LASSO produces a sparse model by shrinking some coefficients and setting most other coefficients to zero. In other words, the LASSO algorithm removes the irrelevant variables (wavelengths in our application). Hence, LASSO produces an interpretable model with only relevant variables, and it also shows high prediction accuracy in many examples [62], [63].

We applied the LASSO method to the logistic regression model for mineral classification. The LASSO regression coefficients in logistic regression can be obtained by minimizing the

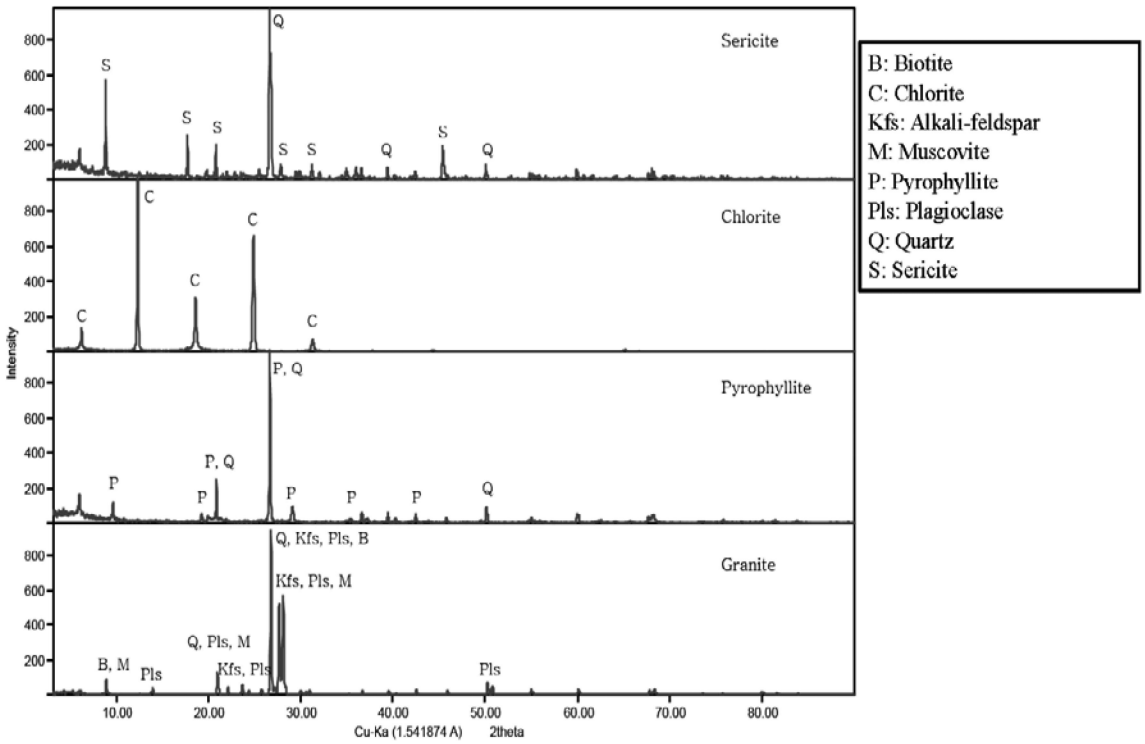

Fig. 1. XRD result of sericite, chlorite, pyrophyllite, and granite.

following LASSO penalized log-likelihood

$$\ell(\beta_0,\ \beta_1, \cdots,\ \beta_p) + \lambda \sum_{j=1}^{p} |\beta_j| \tag{1}$$

where the left term is the negative log-likelihood in logistic regression and the right term is the LASSO penalty. The lambda is the regularization parameter that controls the model complexity, which is often called the tuning parameter to be selected additionally. We select the tuning parameter lambda by a ten-fold cross validation. We used the glmnet() package in *R* for estimating LASSO logistic regression model. Like the logistic regression, the mineral classification can be done by the estimated probability from the LASSO logistic regression.

The spectral indices for detection of sericite, chlorite, and pyrophyllite were derived by logistic regressions with LASSO using training data selected by RF models based on 70% of sample spectra for each case. The derived indices were validated with 30% of sample spectra and spectral library, and the accuracy of the index for each mineral content was analyzed for assessment of efficiency of mineral detection.

III. Result and Discussion

A. Validation of Target Mineral and Granite Samples

The alteration mineral samples used in this article were validated with the XRD analysis. The XRD analysis of the sericite samples showed peaks of muscovite and quartz (see Fig. 1). The sericite is a commonly used term for fined grained white micas produced by hydrothermal alteration and made of muscovite, illite, or paragonite [64]. The XRD peaks confirms the samples are mainly composed of sericite with quartz as a minor mineral. Because the hydrothermal activity accompanies high silicate solutions and quartz is the main gangue mineral, the sericite commonly occurs with quartz. The XRD peaks for chlorite samples indicated pure chlorite samples (see Fig. 1). Pyrophyllite sample showed XRD peaks of pyrophyllite as major component with quartz as a minor. The XRD results found plagioclase, alkali-feldspar, quartz, biotite, and muscovite for granite sample, which are the major rock forming minerals of granite (see Fig. 1).

The additional validation of granite sample based on microscopic observation confirmed the XRD result where QAP diagram defined the sample as a granite with quartz 42%, alkali-feldspar 62%, and plagioclase 38% ([65], Fig. S-1).

B. Spectral Characteristics of Target Mineral Samples

1) Spectral Characteristics of Granite: The granite sample is composed of diverse rock forming minerals, such as feldspar, plagioclase, quartz, biotite, and muscovite, which is common in granite in general. The spectral characteristics of rock forming minerals are featureless in the VNIR-SWIR region [see Fig. 2(a) and (b)] other than muscovite. The spectra of the sample also show featureless spectral characteristics with minimal overlap with muscovite spectrum. It indicates the content of muscovite in the granite sample is minimal. Therefore, the spectral signals of hydrothermal alteration minerals can be easily distinguishable from granite spectra [see Fig. 2(a) and (b)].

2) Spectral Characteristics of Sericite Samples: The spectral characteristics associated various mineral content mixed with granite samples were analyzed. The reflectance and

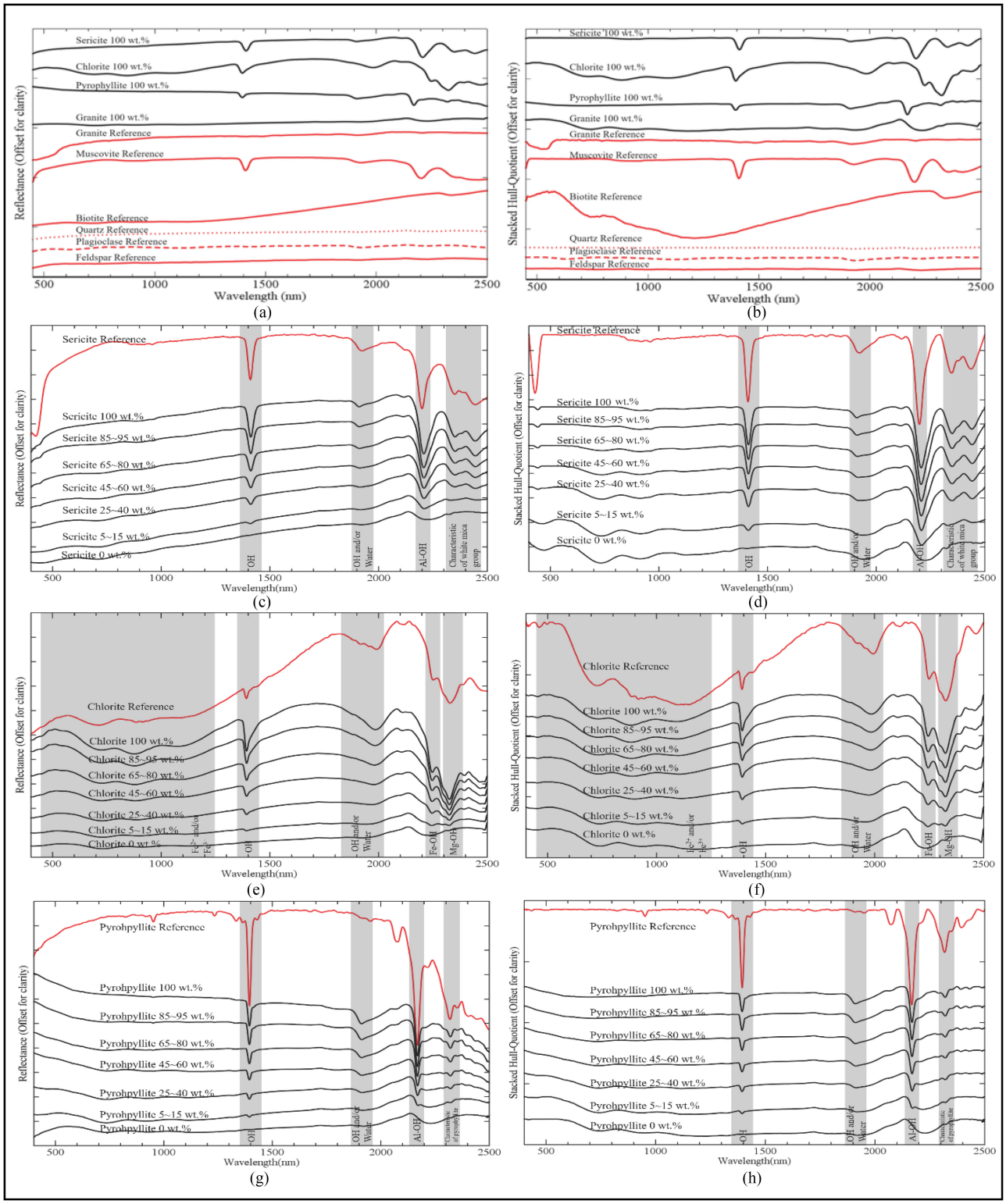

Fig. 2. Reflectance (a), (c), (e), and (g) and Hull-Quotient corrected (b), (d), (f), and (h) spectrum of granite sample plotted with library spectra of major rock forming minerals, and sericite, chlorite, and pyrophyllite at various weight percentage mixed with granite samples.

hull-quotient spectra of sericite samples with content 0 wt.%, 5–20 wt.%, 25–40 wt.%, 45–60 wt.%, 65–80 wt.%, 85–95 wt.%, and 100 wt.% showed systematic variations in absorption features at 1410 nm of OH, 1910 nm of OH/H_2O, 2210 nm of Al-OH, and doublet absorptions at 2342–2435 nm of white mica. The sericite spectrum of 100% samples is identical with the library spectrum confirming the mineral identity. As the sericite content decreased, absorption depths at 1410 nm, 1910 nm, 2210 nm, and 2342–2435 nm decreased accordingly. Notably, the absorption features at 5–15 wt.% sericite content still showed

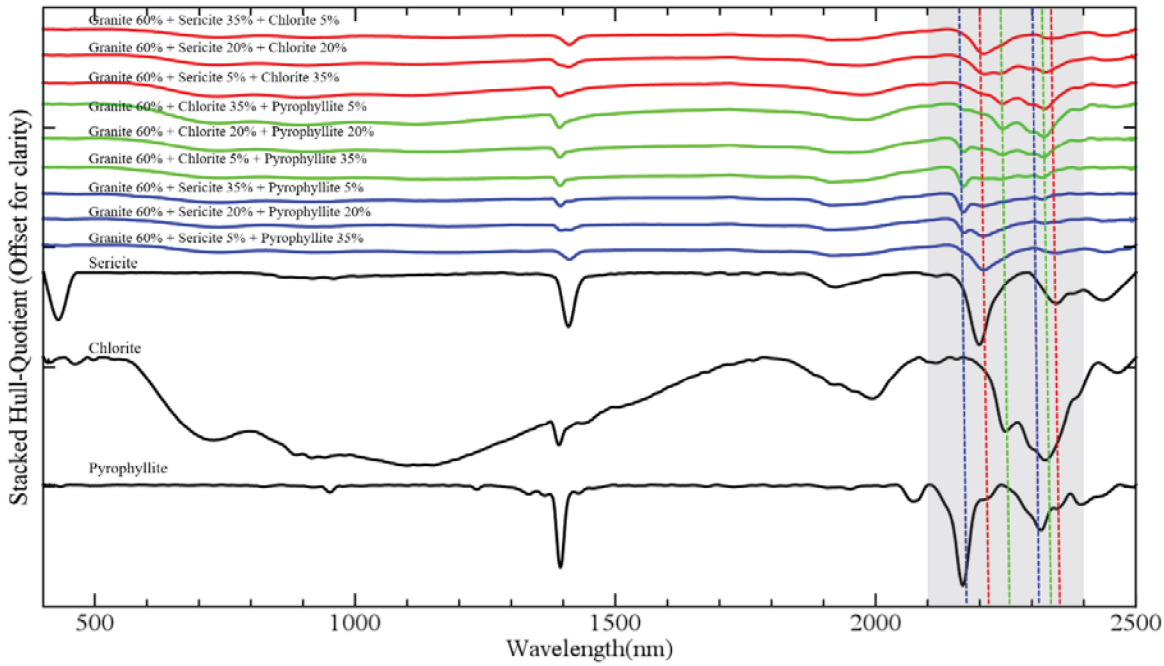

Fig. 3. Hull-Quotient corrected spectra of granite and two types of hydrothermal alteration minerals mixed in various contents red for sericite and chlorite, green for chlorite and pyrophyllite, blue for sericite and pyrophyllite, and black for library reference spectra.

absorption features of white mica and H_2O compared to 0% sample spectrum [see Fig. 2(c) and (d)].

3) Spectral Characteristics of Chlorite Samples: The reflectance and hull-quotient spectra of chlorite samples at 100 wt.% showed distinctive absorption features at 1395 nm of OH, 1990 nm of OH/H_2O, 2245 nm of Fe-OH, and 2325 nm of Mg-OH [47], [66]. The chlorite sample spectrum and library spectrum were identical, confirming the mineral identity in addition to XRD data. As the mineral content decreased, the absorption features weakened systematically. The absorption features of OH/H_2O disappeared at 5–15 wt.%, and the absorption features of OH, Fe-OH and Mg-OH were barely visible at 5–15 wt.% compared to 0 wt.% spectrum [see Fig. 2(e) and (f)].

4) Spectral Characteristics of Pyrophyllite Samples: The reflectance and hull-quotient spectra of pyrophyllite samples at 100 percent showed distinctive features at 1395 nm of OH, 1910 nm OH/H_2O, 2165 nm of Al-OH, and 2319 nm of pyrophyllite characteristic spectra [67]. The pyrophyllite sample spectrum were identical to the USGS spectral library, which confirms the XRD data. As the content of pyrophyllite decreased, the absorption features weakened systematically. The absorption features of OH/H_2O disappeared at 5–15 wt.%, and those of OH, Al-OH and characteristic feature of pyrophyllite weakly survived at 5–15 wt.% compared to 0 wt.% spectrum [see Fig. 2(g) and (h)].

5) Spectral Characteristics of Granite Mixed With Two or Three Types of Hydrothermal Alteration Minerals: The spectral characteristics of mixtures of two or three hydrothermal alteration minerals from 5% to 35% with granite samples were analyzed. The mixtures of sericite and chlorite samples showed systematic decrease of absorption features of the two minerals as a decrease in weight percent (see Fig. 3). The absorption features of sericite at 2210 and 2435 nm were strong at 35 wt.% and barely visible at 5 wt.%. The absorption features of chlorite were observed at 2245 and 2325 nm from 35 wt.% to 5 wt.% (see Fig. 3). When both were at 20 wt.%, the absorption features of both minerals were present at 2210, 2245, 2325, and 2435 nm. The mixtures of chlorite and pyrophyllite also showed systematic decrease in absorption depth which survived at 5 wt.% at 2245 nm for chlorite and 2165 nm for pyrophyllite. The mixtures of sericite and pyrophyllite also showed the same pattern (see Fig. 3).

The mixtures of three alteration minerals also showed systematic changes in absorption features of the three minerals from 20 wt.% to 5 wt.% (see Fig. 4). There were distinctive differences in absorption positions changing in absorption features with their content. Minimum content of 5 wt.% is detectable by the spectrometer. To summarize, based on the wavelengths of the absorption features, this study tested these spectral bands for classifying the mineral mixtures using RF classification algorithm and propose mineral indices that are best for the classification. Furthermore, these indices were included in a LASSO-logistic regression analysis to detect the trace of the three minerals with a minimum content of 5 wt.%.

C. Training Data Selection for Detection Models of Hydrothermal Alteration Minerals

A classification model is commonly developed based on the training data and, thus, the quality of the training data is the most critical factor for target detection. Therefore, optimal selection of the training data is required for model development. This article tested the classification accuracy using training data from library spectra for total of 21 training cases to select optimal

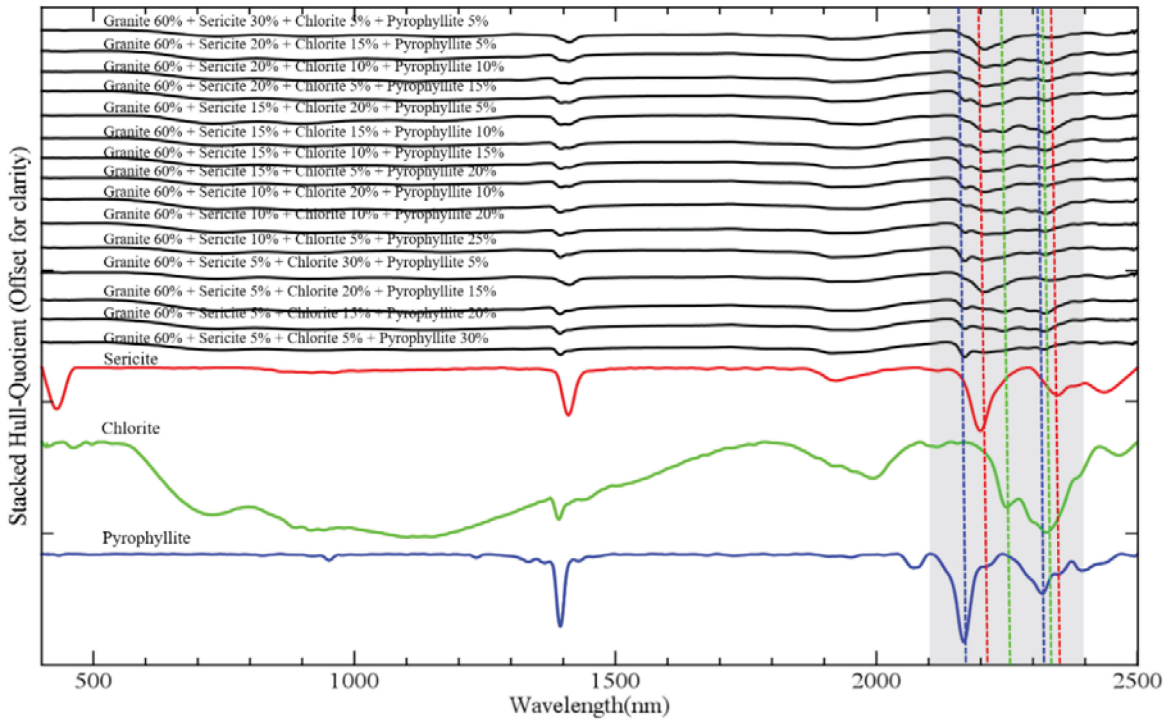

Fig. 4. Hull-Quotient corrected spectra of granite and all three types of target hydrothermal alterated minerals mixed in various contents. Red vertical line for sericite absorption depth, green for chlorite absorption depth, blue for pyrophyllite absorption depth.

training data for detection of each mineral at 5 wt.% or more. The classification results were assessed by detection accuracy of each alteration mineral (omission error) and nonalteration mineral from the library data (commission error). Finally, the optimal training dataset was defined for the derivation of mineral indices. The RF classification was based on 70% of each mineral data, and the rest 30% and library data were used for validation.

The results showed that all classification model showed good accuracy on detection of nontarget minerals with the commission error less than 3%. It indicated that the model is good enough for exclusion of other types of minerals in the library data. The overall accuracy of the classification models was over 70% for all cases (see Table III). However, this number was significantly biased by low commission error. Omission error is misclassification of target mineral into nontarget mineral. Training data strongly affect the omission error because if the model is trained mostly with high mineral content, it tends to omit the low content samples as they were weighted less in the model The omission error was large when the training data was constructed with the library data. The omission errors range from 85% to 93.3% for all three minerals. It indicates that the model cannot detect any real-world samples if the target mineral is mixed with other minerals. The omission error was acceptable when the training data were constructed from 25 wt.% or more, where the error was 31.2% for sericite, 29.3% for chlorite, and 34.3% for pyrophyllite, respectively (see Table III). The best classification results had an overall accuracy higher than 97% when the training data was constructed from the samples with 5 wt.% or more including the library data. The omission error for those models was 2.3% for sericite, 4.0% for chlorite, and 3.7% for pyrophyllite. With more mineral mixture, the omission error decreased slightly. An explanation is the low mineral content is more easily omitted by the model trained with high mineral content. Unless the model is specifically trained with low mineral content, it will not detect some minerals if their portion is lower than a certain threshold. It concludes that the model trained by the data including all mineral samples and library data would have the highest efficiency in target mineral detection. Therefore, this article derived mineral indices for target mineral detection using the training data with mineral samples with 5 wt.% or more including the library data based on LASSO-logistic regression model.

The contribution of the spectral bands at different wavelengths to the classification was evaluated as Gini index. The higher the index, the more important the variable is. From Fig. 5, we can see the most important bands for pyrophyllite are the bands near the absorption feature of Al-OH at 2158–2177 nm. The most important bands for Sericite detection include the features of Al-OH at 2158–2177 nm and 2196–2222 nm. The important bands for chlorite are located at 2293–2336 nm by Mg-OH and 2196–2222 nm by Al-OH. These absorption features have minimal overlap each other where the absorption features are valid with 5 wt.% content.

D. Detection Index of the Hydrothermal Alteration Minerals From LASSO Logistic Regression

The RF model had the best accuracy with training data at 5 wt.% mineral content. The mineral indices of sericite, chlorite, and pyrophyllite with detection capabilities of 5 wt.% or more mineral content were derived from LASSO-logistic regression

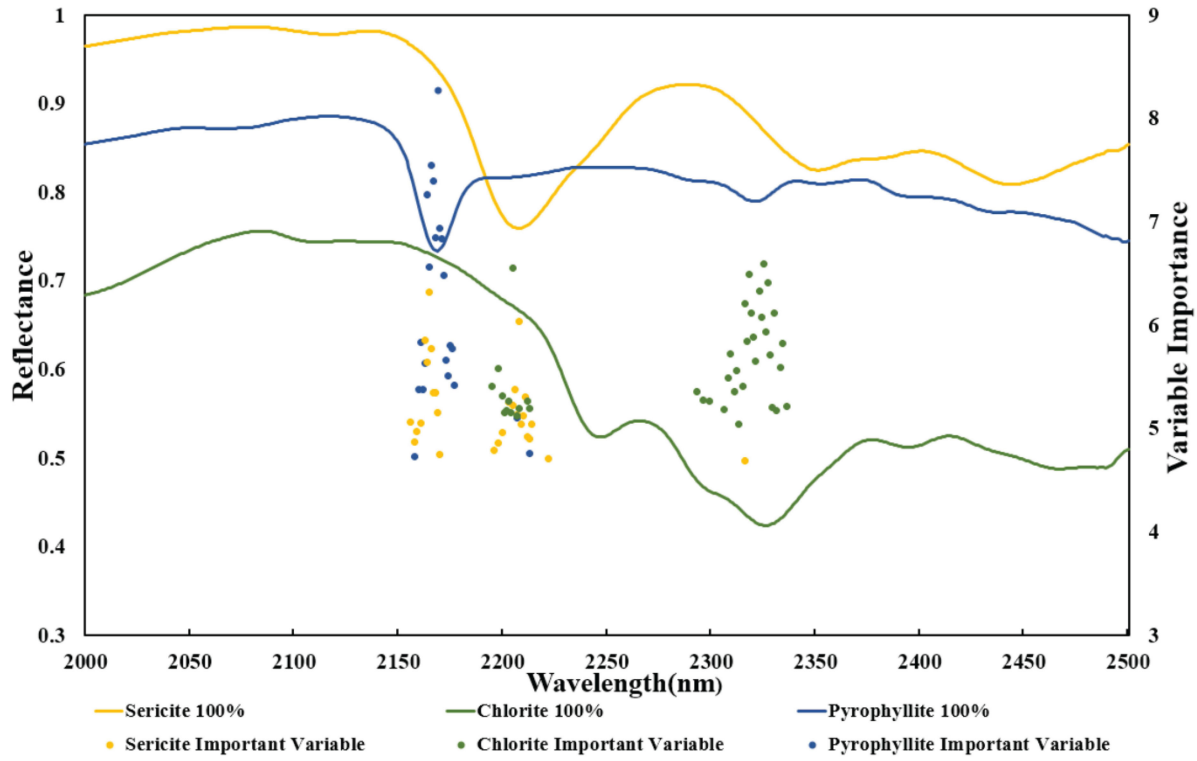

Fig. 5. Top 40 important spectral variables for target mineral classification derived from RF overlaid with reflectance spectra of sericite, chlorite and pyrophyllite from 2000 to 2500 nm.

TABLE IV
ACCURACY ASSESSMENT OF TRAINING AND VALIDATION DATA FOR INDICES DERIVED FROM LASSO-LOGISTIC REGRESSION MODEL

	Target Minerals		
Accuracy Assessment	Sericite	Chlorite	Pyrophyllite
Validation Set Overall accuracy[%]	95.3	94.1	99.5
Validation Set Omission Error[%]	13.9	14.1	2.0
Validation Set Commission Error[%]	1.2	2.7	0.0
RMSE of Validation Set	0.28	0.30	0.24
R^2 of Validation Set	0.62	0.57	0.71

based on the training data with mineral content ranging from 5 wt.% to 100 wt.%. The model was constructed based on 70% of the mineral spectra including the sample spectra of this study and library spectra, and the rest 30% were used for validation of the indices. To evaluate if the trained model can work with real-world cases, the nontarget mineral spectra were used to assess the performance of the models.

As a result, the detection indices were derived by employing spectral variables of 82 bands for sericite, 132 bands for chlorite, and 84 bands for pyrophyllite (see Table S-1). The spectral variables of sericite index include Al-OH absorption bands from 2148 to 2248 nm and sericite absorption bands from 2339 to 2447 nm. Those of chlorite indices include Fe-OH absorption bands from 2222 to 2282 nm and Mg-OH absorption bands from 2295 to 2379 nm. Those of pyrophyllite indices include Al-OH absorption bands from 2149 to 2195 and pyrophyllite absorption from 2303 to 2344 nm. The overall accuracy of the models for calibration data were from 93.6% for chlorite to 99.1% for pyrophyllite and the R^2 values were from 0.65 for chlorite to 0.71 for pyrophyllite (see Table IV). The models showed excellent accuracy on detection on nontarget minerals with commission error from 0.0% to 3.1%, and the detection error of target minerals were from 3.1% to 14.1%. All assessment parameters of training data showed that the models performed well in detection of target minerals with various weight content.

The models' accuracy assessment on validation data also showed an outstanding model performance with the overall accuracy of 94.1% to 99.5%, which was even better than the cross-validation in the training data. The detection error of the models on nontarget minerals was 0.0% to 2.7% and that on target minerals was 2.0% to 14.1%. The R^2 values of the models on validation data were 0.57 to 0.71 (see Table IV).

The models' performance coincided well with the training data showing excellent statistical significance.

This article introduced the quantity-controlled detection indices of sericite, chlorite, and pyrophyllite, which are representative alteration minerals of phyllic, propylitic, and advanced argillic hydrothermal alteration, respectively. While the previous studies did not provide detection threshold in terms of weight content [27], [28], [32], [34], [35], [37], [39], [40], this study defined the detection threshold at 5 wt.% for each target mineral. The quantity-controlled indices provide higher reliability on real-world applications as the models were both tested by machine learning and LASSO-regression analysis with high statistical significance. Moreover, the models were tested not only for the target minerals, but also for the nontarget minerals resulting higher applicability in the real-world cases. Given the fact that the models were constructed with nonatmospheric bands, it can be used not only for ground-based spectroscopic analyses but also on the hyperspectral images acquired from UAVs. We expect that these models will be widely adopted in mineral exploration applications because of the association of phyllic, propylitic, advanced argillic alteration zones with high-value resources such as epithermal gold deposit, iron-oxide-copper-gold deposit, volcanogenic massive sulphide, and porphyry copper ore deposits.

IV. Conclusion

This article introduces spectral indices for hydrothermal mineral detection including sericite, chlorite, and pyrophyllite, the representative alteration minerals of phyllic, propylitic, and advanced argillic hydrothermal alterations, with consideration of mineral combination at various amount of mixture with granite, the representative rock containing major rock forming minerals. The XRD analysis and microscopic observation confirmed the identity of mineral and granite samples where sample minerals contain quartz as a minor mineral. The absorption depths of target minerals systematically decreased with decrease in the mineral content, while the decrease patterns varied by the mineral types. The absorption features of sericite at 2210 and 2435 nm are clearly detectable at 35 wt.% and barely diminished at 5 wt.%. The absorption features of chlorite were detectable at 2245 and 2325 nm from 35 wt.% to 5 wt.%. The absorption features of pyrophyllite at 2165 nm survived at all levels of the mineral content.

The RF model is used to select the most effective spectra for the target mineral content detection ranging from 35% to 5%. The results showed that the commission error of all classification model was very low less than 3%. It indicated that the model is good enough for exclusion of other types of minerals in the library data. However, the omission error was enormously large when the training data was constructed with the mineral samples with higher than 30 wt.%. The best classification model for each of the three minerals showed overall accuracy higher than 97% when the training data were selected from the samples with 5 wt.% or more. It concludes that the training data using the mineral samples with 5 wt.% or more would have the highest efficiency in target mineral detection.

The spectral indices for the target mineral detection were derived by employing spectral variables of 82 bands for sericite, 132 bands for chlorite, and 84 bands for pyrophyllite. The spectral variables of sericite indices include Al-OH absorption bands from 2148 to 2248 nm and sericite absorption bands from 2339 to 2447 nm. Those of chlorite indices include Fe-OH absorption bands from 2222 to 2282 nm and Mg-OH absorption bands from 2295 to 2379 nm. Those of pyrophyllite indices include Al-OH absorption bands from 2149 to 2195 nm and pyrophyllite absorption from 2303 to 2344 nm. The models' performance was excellent showing the overall accuracy higher than 93.6% with R^2 values ranging from 0.57 to 0.71.

This article introduced the quantity-controlled detection indices of sericite, chlorite, and pyrophyllite working at a mineral content higher than 5 wt.%. The quantity-controlled indices provide higher reliability on real-world applications as they were tested with the target minerals as well as the nontarget minerals. Given the fact that the models were constructed with nonatmospheric bands, it can be used not only for ground-based spectroscopic analyses but also on the hyperspectral images acquired from UAVs.

References

[1] R. H. Sillitoe and H. F. Bonham, "Volcanic landforms and ore deposits," *Econ. Geol.,* vol. 79, no. 6, pp. 1286–1298, 1984.

[2] J. W. Hedenquist and J. B. Lowenstern, "The role of magmas in the formation of hydrothermal ore deposits," *Nature,* vol. 370, no. 6490, pp. 519–527, 1994.

[3] M. Jébrak, "Hydrothermal Breccias in vein-type ore deposits: A review of mechanisms, morphology and size distribution," *Ore Geol. Rev.,* vol. 12, no. 3, pp. 111–134, 1997.

[4] J. Sánchez-España, F. Velasco, and I. Yusta, "Hydrothermal alteration of felsic volcanic rocks associated with massive sulphide deposition in the northern iberian pyrite belt (SW spain)," *Appl. Geochemistry,* vol. 15, no. 9, pp. 1265–1290, 2000.

[5] M. L. Zientek and G. J. Orris, "Geology and nonfuel mineral deposits of the United States," US Geological Surv., Reston, VA, USA, 2005.

[6] A. Thompson, J. Thompson, and K. Dunne, "Atlas of alteration: A field and petrographic guide to hydrothermal alteration minerals. Geological association of Canada," *Mineral Deposits Division,* vol. 120, 1996.

[7] A. B. Pour and M. Hashim, "Identification of hydrothermal alteration minerals for exploring of porphyry copper deposit using ASTER data, SE Iran," *J. Asian Earth Sci.,* vol. 42, no. 6, pp. 1309–1323, 2011.

[8] A. R. Mokhtari, "Hydrothermal alteration mapping through multivariate logistic regression analysis of lithogeochemical data," *J. Geochemical Exploration,* vol. 145, pp. 207–212, 2014.

[9] M. J. Heap, D. M. Gravley, B. M. Kennedy, H. A. Gilg, E. Bertolett, and S. L. Barker, "Quantifying the role of hydrothermal alteration in creating geothermal and epithermal mineral resources: The Ohakuri ignimbrite (Taupō volcanic zone, New Zealand)," *J. Volcanol. Geothermal Res.,* vol. 390, 2020, Art. no. 106703.

[10] F. Pirajno, "Hydrothermal processes and wall rock alteration," in *Hydrothermal Processes and Mineral Systems*, Berlin, Germany: Springer, 2009, pp. 73–164.

[11] L. Mathieu, "Quantifying hydrothermal alteration: A review of methods," *Geosciences,* vol. 8, no. 7, pp. 1–27, 2018.

[12] C. Phillips, N. Gambell, and D. Fountain, "Hydrothermal alteration, mineralization, and zoning in the ray deposit," *Econ. Geol.,* vol. 69, no. 8, pp. 1237–1250, 1974.

[13] A. Kishida and R. Kerrich, "Hydrothermal alteration zoning and gold concentration at the Kerr-Addison archean lode gold deposit, Kirkland lake, Ontario," *Econ. Geol.,* vol. 82, no. 3, pp. 649–690, 1987.

[14] L. V. Monteiro *et al.*, "Spatial and temporal zoning of hydrothermal alteration and mineralization in the sossego iron oxide–copper–gold deposit, carajás mineral province, Brazil: Paragenesis and stable isotope constraints," *Mineralium Deposita,* vol. 43, no. 2, pp. 129–159, 2008.

[15] A. B. Pour, M. Hashim, and J. van Genderen, "Detection of hydrothermal alteration zones in a tropical region using satellite remote sensing data: Bau goldfield, Sarawak, Malaysia," *Ore Geol. Rev.,* vol. 54, pp. 181–196, 2013.

[16] J. W. Hedenquist, A. Arribas, and E. Gonzalez-Urien, "Exploration for epithermal gold deposits," *Rev. Econ. Geol.,* vol. 13, no. 2, pp. 45–77, 2000.

[17] A. C. Harris and S. D. Golding, "New evidence of magmatic-fluid–related phyllic alteration: Implications for the genesis of porphyry cu deposits," *Geology,* vol. 30, no. 4, pp. 335–338, 2002.

[18] D. Norman, W. Parry, and J. R. Bowman, "Petrology and geochemistry of propylitic alteration at southwest tintic, Utah," *Econ. Geol.,* vol. 86, no. 1, pp. 13–28, 1991.

[19] R. H. Sillitoe, "Porphyry copper systems," *Econ. Geol.,* vol. 105, no. 1, pp. 3–41, 2010.

[20] M. N. Cagatay, "Hydrothermal alteration associated with volcanogenic massive sulfide deposits; examples from Turkey," *Econ. Geol.,* vol. 88, no. 3, pp. 606–621, 1993.

[21] Z. Zhang, J. Mao, Y. Wang, F. Pirajno, J. Liu, and Z. Zhao, "Geochemistry and geochronology of the volcanic rocks associated with the dong'an adularia–sericite epithermal gold deposit, lesser hinggan range, heilongjiang province, NE China: Constraints on the metallogenesis," *Ore Geol. Rev.,* vol. 37, no. 3/4, pp. 158–174, 2010.

[22] A. B. Pour and M. Hashim, "The application of ASTER remote sensing data to porphyry copper and epithermal gold deposits," *Ore Geol. Rev.,* vol. 44, pp. 1–9, 2012.

[23] M. H. Zadeh, M. H. Tangestani, F. V. Roldan, and I. Yusta, "Spectral characteristics of minerals in alteration zones associated with porphyry copper deposits in the middle part of Kerman copper belt, SE Iran," *Ore Geol. Rev.,* vol. 62, pp. 191–198, 2014.

[24] A. B. Pour and M. Hashim, "Hydrothermal alteration mapping from landsat-8 data, sar cheshmeh copper mining district, south-eastern Islamic republic of Iran," *J. Taibah Univ. Sci.,* vol. 9, no. 2, pp. 155–166, 2015.

[25] X. Zhou, C. Jara, M. Bardoux, and C. Pasencia, "Multi-scale integrated application of spectral geology and remote sensing for mineral exploration," in *Proc. 6th Decennial Int. Conf. Mineral Exploration*, 2017, pp. 21–25.

[26] M. Safari, A. Maghsoudi, and A. B. Pour, "Application of landsat-8 and ASTER satellite remote sensing data for porphyry copper exploration: A case study from Shahr-e-Babak, kerman, south of Iran," *Geocarto Int.,* vol. 33, no. 11, pp. 1186–1201, 2018.

[27] A. Salimi, M. Ziaii, M. Hosseinjani Zadeh, A. Amiri, and S. Karimpouli, "High performance of the support vector machine in classifying hyperspectral data using a limited dataset," *Int. J. Mining Geo-Eng.,* vol. 49, no. 2, pp. 253–268, 2015.

[28] M. Abdolmaleki, N. Fathianpour, and M. Tabaei, "Evaluating the performance of the wavelet transform in extracting spectral alteration features from hyperspectral images," *Int. J. Remote Sens.,* vol. 39, no. 19, pp. 6076–6094, 2018.

[29] H. Govil, N. Gill, S. Rajendran, M. Santosh, and S. Kumar, "Identification of new base metal mineralization in Kumaon Himalaya, India, using hyperspectral remote sensing and hydrothermal alteration," *Ore Geol. Rev.,* vol. 92, pp. 271–283, 2018.

[30] F. J. Testa, C. Villanueva, D. R. Cooke, and L. Zhang, "Lithological and hydrothermal alteration mapping of epithermal, porphyry and tourmaline breccia districts in the argentine andes using ASTER imagery," *Remote Sens.,* vol. 10, no. 2, pp. 1–45, 2018.

[31] F. A. Kruse, R. L. Bedell, J. V. Taranik, W. A. Peppin, O. Weatherbee, and W. M. Calvin, "Mapping alteration minerals at prospect, outcrop and drill core scales using imaging spectrometry," *Int. J. Remote Sens.,* vol. 33, no. 6, pp. 1780–1798, 2012.

[32] Y. E. Molan, D. Refahi, and A. H. Tarashti, "Mineral mapping in the Maherabad area, eastern Iran, using the hymap remote sensing data," *Int. J. Appl. Earth Observ. Geoinf.,* vol. 27, pp. 117–127, 2014.

[33] M. K. Tripathi and H. Govil, "Evaluation of AVIRIS-NG hyperspectral images for mineral identification and mapping," *Heliyon,* vol. 5, no. 11, 2019, Art. no. e02931.

[34] S. Jakob, R. Zimmermann, and R. Gloaguen, "The need for accurate geometric and radiometric corrections of drone-borne hyperspectral data for mineral exploration: Mephysto—A toolbox for pre-processing drone-borne hyperspectral data," *Remote Sens.,* vol. 9, no. 1, pp. 1–17.

[35] M. Kirsch *et al.*, "Integration of terrestrial and drone-borne hyperspectral and photogrammetric sensing methods for exploration mapping and mining monitoring," *Remote Sens.,* vol. 10, no. 9, pp. 1–31, 2018.

[36] F. Kruse, "Identification and mapping of minerals in drill core using hyperspectral image analysis of infrared reflectance spectra," *Int. J. Remote Sens.,* vol. 17, no. 9, pp. 1623–1632, 1996.

[37] G. Taylor, "Mineral and lithology mapping of drill core pulps using visible and infrared spectrometry," *Natural Resour. Res.,* vol. 9, no. 4, pp. 257–268, 2000.

[38] A. Kerr, H. Rafuse, G. Sparkes, J. Hinchey, and H. Sandeman, "Visible/infrared spectroscopy (VIRS) as a research tool in economic geology: Background and pilot studies from Newfoundland and Labrador," *Geolog. Surv. Rep.,* vol. 11, pp. 145–166, 2011.

[39] W. M. Calvin and E. L. Pace, "Mapping alteration in geothermal drill core using a field portable spectroradiometer," *Geothermics,* vol. 61, pp. 12–23, 2016.

[40] I. C. C. Acosta, M. Khodadadzadeh, L. Tusa, P. Ghamisi, and R. Gloaguen, "A machine learning framework for drill-core mineral mapping using hyperspectral and high-resolution mineralogical data fusion," *IEEE J. Sel. Topics Appl. Earth Observ. Remote Sens.,* vol. 12, no. 12, pp. 4829–4842, Dec. 2019.

[41] K. Pazand, J. F. Sarvestani, and M. R. S. Ravasan, "Hydrothermal alteration mapping using ASTER data for reconnaissance porphyry copper mineralization in the Ahar area, NW Iran," *J. Indian Soc. Remote Sens.,* vol. 41, no. 2, pp. 379–389, 2013.

[42] Y.-S. Son, M.-K. Kang, and W.-J. Yoon, "Lithological and mineralogical survey of the Oyu Tolgoi region, Southeastern Gobi, Mongolia using ASTER reflectance and emissivity data," *Int. J. Appl. Earth Observ. Geoinf.,* vol. 26, pp. 205–216, 2014.

[43] Y.-S. Son, M.-K. Kang, and W.-J. Yoon, "Pyrophyllite mapping in the Nohwa deposit, Korea, using ASTER remote sensing data," *Geosci. J.,* vol. 18, no. 3, pp. 295–305, 2014.

[44] J. H. Shin, J. Yu, L. Wang, J. Kim, S.-M. Koh, and S.-O. Kim, "Spectral responses of heavy metal contaminated soils in the vicinity of a hydrothermal ore deposit: A case study of Boksu mine, South Korea," *IEEE Trans. Geosci. Remote Sens.,* vol. 57, no. 6, pp. 4092–4106, Jun. 2019.

[45] Y. Jeong, J. Yu, L. Wang, H. Shin, S.-M. Koh, and G. Park, "Cost-effective reflectance calibration method for small UAV images," *Int. J. Remote Sens.,* vol. 39, no. 21, pp. 7225–7250, 2018.

[46] K. Yang, P. Browne, J. Huntington, and J. Walshe, "Characterising the hydrothermal alteration of the broadlands–Ohaaki geothermal system, New Zealand, using short-wave infrared spectroscopy," *J. Volcanol. Geothermal Res.,* vol. 106, no. 1/2, pp. 53–65, 2001.

[47] W. Herrmann *et al.*, "Short wavelength infrared (SWIR) spectral analysis of hydrothermal alteration zones associated with base metal sulfide deposits at Rosebery and western Tharsis, Tasmania, and highway-reward, Queensland," *Econ. Geol.,* vol. 96, no. 5, pp. 939–955, 2001.

[48] J. B. Percival *et al.*, "Customized spectral libraries for effective mineral exploration: Mining national mineral collections," *Clays Clay Minerals,* vol. 66, no. 3, pp. 297–314, 2018.

[49] J. Hinchey, "Visible/infrared spectroscopy (VIRS) of volcanogenic massive sulphide hydrothermal alteration products, tulks volcanic belt, central newfoundland: An additional exploration technique?," *Geolog. Surv. Rep.,* vol. 11, pp. 97–108, 2011.

[50] Y. Jeong, J. Yu, S.-M. Koh, C.-H. Heo, and J. Lee, "Spectral characteristics of minerals associated with skarn deposits: A case study of weondong skarn deposit, South Korea," *Geosci. J.,* vol. 20, no. 2, pp. 167–182, 2016.

[51] A. M. Baldridge, S. Hook, C. Grove, and G. Rivera, "The ASTER spectral library version 2.0," *Remote Sens. Environ.,* vol. 113, no. 4, pp. 711–715, 2009.

[52] R. F. Kokaly *et al.*, "USGS spectral library version 7," US Geolog. Surv., Reston, VA, USA, 2017.

[53] P. Shippert, "Introduction to hyperspectral image analysis," *Online J. Space Commun.,* vol. 3, pp. 1–13, 2003.

[54] L. Breiman, "Random forests," *Mach. Learn.,* vol. 45, no. 1, pp. 5–32, 2001.

[55] L. Guo, N. Chehata, C. Mallet, and S. Boukir, "Relevance of airborne lidar and multispectral image data for urban scene classification using random forests," *ISPRS J. Photogramm. Remote Sens.,* vol. 66, no. 1, pp. 56–66, 2011.

[56] V. F. Rodriguez-Galiano, B. Ghimire, J. Rogan, M. Chica-Olmo, and J. P. Rigol-Sanchez, "An assessment of the effectiveness of a random forest classifier for land-cover classification," *ISPRS J. Photogramm. Remote Sens.,* vol. 67, pp. 93–104, 2012.

[57] H. Han, X. Guo, and H. Yu, "Variable selection using mean decrease accuracy and mean decrease Gini based on random forest," in *Proc. 7th IEEE Int. Conf. Softw. Eng. Service Sci.*, 2016, pp. 219–224.

[58] M. L. Calle and V. Urrea, "Letter to the editor: Stability of random forest importance measures," *Briefings Bioinformatics,* vol. 12, no. 1, pp. 86–89, 2011.
[59] P. O. Gislason, J. A. Benediktsson, and J. R. Sveinsson, "Random forests for land cover classification," *Pattern Recognit. Lett.,* vol. 27, no. 4, pp. 294–300, 2006.
[60] L. C. Rowan, R. G. Schmidt, and J. C. Mars, "Distribution of hydrothermally altered rocks in the reko diq, Pakistan mineralized area based on spectral analysis of ASTER data," *Remote Sens. Environ.,* vol. 104, no. 1, pp. 74–87, 2006.
[61] B. Chung *et al.*, "Detection of magnesite and associated gangue minerals using hyperspectral remote sensing—A laboratory approach," *Remote Sens.,* vol. 12, no. 8, pp. 1–26, 2020.
[62] M. Dyar, M. Carmosino, E. Breves, M. Ozanne, S. Clegg, and R. Wiens, "Comparison of partial least squares and Lasso regression techniques as applied to laser-induced breakdown spectroscopy of geological samples," *Spectrochimica Acta Part B, Atomic Spectrosc.,* vol. 70, pp. 51–67, 2012.
[63] S. Lee, Y. Pawitan, E. Ingelsson, and Y. Lee, "Sparse estimation of gene–gene interactions in prediction models," *Statist. Methods Med. Res.,* vol. 26, no. 5, pp. 2319–2332, 2017.
[64] W. D. Nesse, *Introduction to Mineralogy*, 2nd ed., New York, NY, USA: Oxford Univ. Press, 2012.
[65] S. Baxter and M. Feely, "Magma mixing and mingling textures in granitoids: Examples from the galway granite, connemara, Ireland," *Mineral. Petrol.,* vol. 76, no. 1/2, pp. 63–74, 2002.
[66] P. Hauff, "An overview of VIS-NIR-SWIR field spectroscopy as applied to precious metals exploration," *Spectral Int. Inc.,* vol. 80001, pp. 303–403, 2008.
[67] P. Bierwirth, D. Huston, and R. Blewett, "Hyperspectral mapping of mineral assemblages associated with gold mineralization in the central Pilbara, western Australia," *Econ. Geol.,* vol. 97, no. 4, pp. 819–826, 2002.

Kyuhun Shim received the B.S. degree in geology and earth environmental sciences in 2018 from the Chungnam National University, Daejeon, South Korea, where he is currently working of M.S. degree in the Department of Astronomy, Space Science and Geology in subject of remote sensing.

His research interest includes mineral spectroscopy and remote sensing in hydrothermal alteration zones, especially hyperspectral remote sensing about hydrothermal alterated minerals.

Jaehyung Yu received the B.S. degree in geology and M.S. degree in applied geology from Chungnam National University, Daejeon, South Korea, in 1997 and 1999, respectively, and the Ph.D. degree in geography from Texas A&M University, College Station, TX, USA, in 2005.

From 2005 to 2012, he was an Assistant and an Associate Professor with Texas A&M University-Kingsville, Kingsville, TX, USA. He was with the Department of Geological Sciences, Chungnam National University, Daejeon, South Korea, in 2012, and is currently a Professor. His specialty includes UAV and satellite remote sensing applications on geological and environmental processes.

Lei Wang received the Ph.D. degree in geography from the Texas A&M University, College Station, TX, USA, in 2006.

He is currently a Professor with the Department of Geography and Anthropology, Louisiana State University, Baton Rouge, LA, USA. His research interests include remote sensing applications, image analysis, geostatistical models, surface hydrology, and flood hazards.

Sangin Lee received the Ph.D. degree in statistics from Seoul National University, Seoul, South Korea, in 2012.

He is currently an Assistant Professor with the Department of Information and Statistics, Chungnam National University, Daejeon, South Korea. His research interests include high-dimensional statistical modeling, methods and theories for penalized likelihood models, network analysis and integrative analysis, computational statistics.

Sang-Mo Koh received the Ph.D. degree in mineralogy at the Department of Geology, Seoul National University, Seoul, South Korea in 1996.

He is currently the Director of the Convergence Research Center for Development of Mineral Resources, Korea Institute of Geoscience and Mineral Resources, Daejeon, South Korea. His research interests include mineral exploration, genesis of mineral deposits, and potential evaluation of mineral deposits.

Bum Han Lee received the Ph.D. degree in mineralogy at the School of Earth and Environemntal Sciences, Seoul National University, Seoul, South Korea, in 2011.

He is currently a Senior Researcher with the Convergence Research Center for Development of Mineral Resources, Korea Institute of Geoscience and Mineral Resources, Daejeon, South Korea. His recent research interests include the development of exploration technology using the hyperspectral camera and the geochemistry in the ore geneses (Fe, Cu, REE, Pb-Zn, and Mg) and its implications for tectonic evolution in Northeast Asia.